Revista Minelor – Mining Revue
ISSN-L 1220-2053 / ISSN 2247-8590
vol. 31, issue 3, pp. 127-135, selected paper from the First International EnviroMining Virtual Conference 2025

3D MODELING OF WATER INRUSH IN COAL MINES: UNDERSTANDING THE CAUSES TO ENHANCE SAFETY IN MINING OPERATIONS

Jinxi LIANG[1], Sara KASMAEEYAZDI[2],*
Xiaoning LIU[3], Francesco TINTI[4]

[1]School of Resources and Geosciences, China Univ. of Mining and Technology, Xuzhou, Jiangsu, China
[2] Department of Civil, Chemical, Environmental and Materials Engineering, University of Bologna, Italy, sara.kasmaeeyazdi2@unibo.it
[3]School of Earth Sciences and Resources, China University of Geosciences, Bejing, China
[4]Department of Civil, Chemical, Environmental and Materials Engineering, University of Bologna, Italy, francesco.tinti@unibo.it

DOI: 10.2478/minrv-2025-0036
received – 21.01.2025 / revised – 08.02.2025
accepted – 18.02.2025 / published – 22.09.2025

Abstract: *Water-sand mixture inrush disaster in coal underground mining activities refers to the disruption of the original equilibrium state in the source area. This leads to the sudden inflow of water-sand (or water-solid) mixture under its own gravity or pressure into the underground, seeking a new equilibrium. This process often results in significant economic losses and casualties. The present work refers to a disaster happened in China in 2018; during a tunnel excavation of a coal mine, an instantaneous water-solid mixture inrush of around 15,000 m^3/h flooded the work site. By collecting all the available information about the geology and hydrogeology of the area, a 3D geological model was created, from the surface to beyond the depth of the mine. Afterwards, the inrush was numerically simulated and the results were compared with the hydraulic head variations in the area, measured by the nearest piezometer. The results can be used to better understand the water inrush phenomenon, in order to enhance safety of mining operations in similar geological conditions.*
Keywords: *water-sand mixture inrush, co-kriging interpolation, mine water hazards, underground fracture pathways*

1. Introduction

Water-sand mixture flows (WSMFs) pose significant hazards to underground operations, threatening workplace safety, infrastructure stability, and nearby human settlements. Unlike conventional water-related hazards, WSMFs—analogous to underground mudflows or pure sand flows—are characterized by the high sand content within the fluid, which presents unique challenges. These hazards occur naturally worldwide, often unnoticed, but are becoming increasingly impactful due to expanding human activities such as mining, drilling, and underground construction [1, 2]. For instance, in soft soil regions, the movement of WSMF through underground pathways can lead to localized soil erosion and subsurface subsidence. For instance, in May 2023, a borehole penetrating a collapse column in Tianjin, China, triggered WSMF migration, resulting in uneven ground settlement, building tilting, and road cracking, which displaced approximately 4,000 residents (Figure 1a) [3]. Similar disasters have been reported in Florida, USA, the Ural Mountains, Russia, and other regions globally, where underground cavities or collapse columns facilitated WSF migration, causing surface subsidence and infrastructure damage [4, 5].

Mining operations, especially during resource extraction, represent high-frequency scenarios for such disasters [6-9] (Figure 1b). Compared to other disaster-inducing activities, mining offers a unique research advantage: it allows simultaneous observation of surface impacts and subsurface WSMF dynamics. The migration of WSMFs occurs when underground pathways—such as faults [10], boreholes [11], failure zones [8], or fracture networks [12, 13] - connect subsurface spaces with water-sand sources. These pathways, classified as direct, indirect, or combined, facilitate the movement of water-sand mixtures into these underground spaces, driven by gravity and water pressure, disrupting the equilibrium within source zones.

* Corresponding author: Camelia Madear, Lect.Eng. Ph.D., University of Petrosani, Petrosani, Romania, 20, University Street, www.upet.ro, cameliamadear@upet.ro

vol. 31, issue 3 / 2025
pp. 127-135

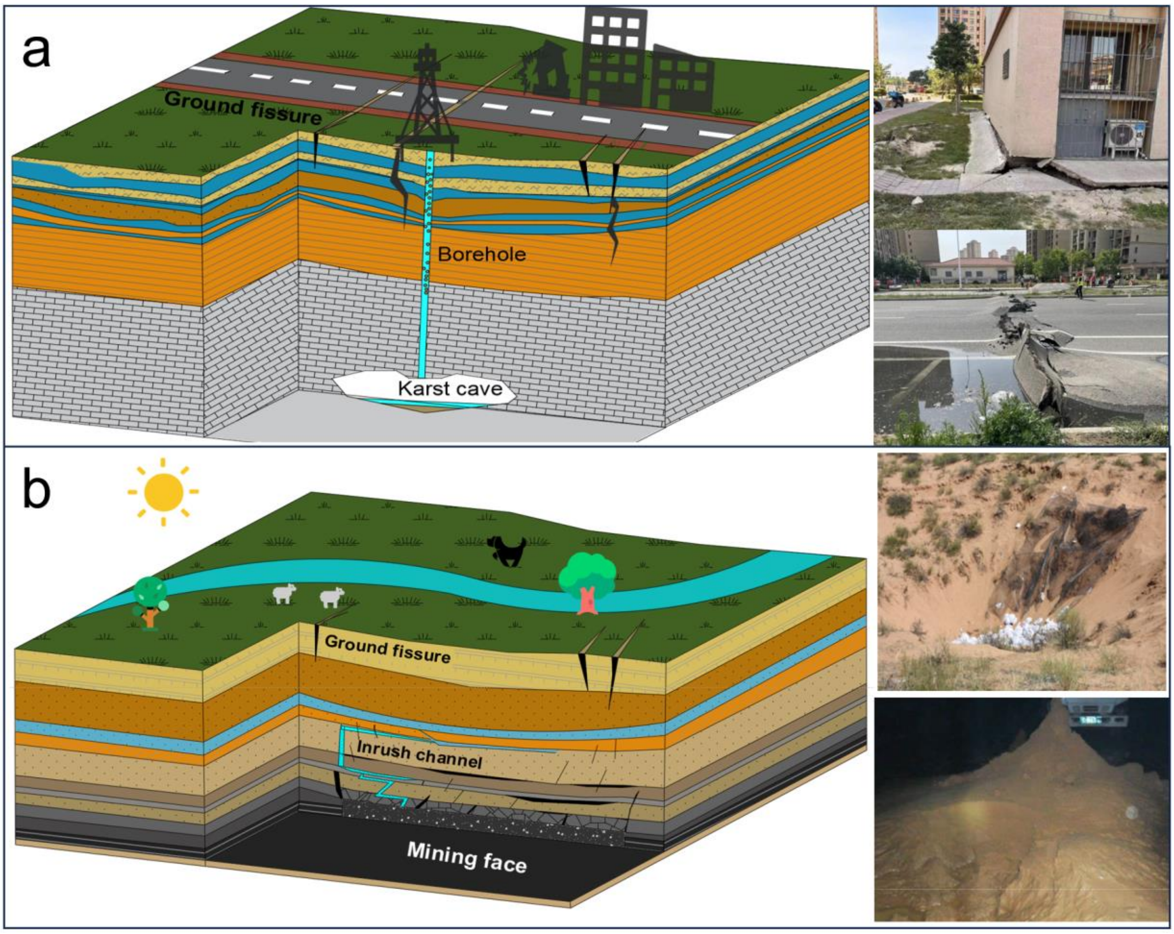

Fig. 1 Three-dimensional schematic diagram (a) WSMF caused by drilling, with photos of surface and building cracks (b) Mining-induced fracture channels causing WSMF, with photos the accident scene and surface collapse

In present, integrating multi-source data and geostatistical techniques for channel inversion in coal mine WSMF disasters remains in the exploratory stage. Accurate identification of potential WSMF migration pathways is critical for disaster prevention and mitigation. However, current tracing methods often lack integration of multi-source data or geostatistical modelling for channel reconstruction.

This study addresses these gaps by integrating field monitoring data, laboratory experiments, 3D modelling and numerical simulations to analyse WSMF migration in coal mines. Specifically, it introduces a new inversion method based on grain size analysis and water level dynamics, constructs a 3D geological model using borehole data, and examines migration patterns under various pathway geometries. The findings aim to advance the understanding of WSMF disaster mechanisms and provide practical guidance for early warning and prevention.

Beyond offering immediate insights, we hope this study serves as a call to action, highlighting the severe hazards of underground water-sand migration. We aim to inspire greater attention to this direction, fostering deeper investigations and practical solutions to mitigate these risks.

2. Methods

2.1. Study area and disaster background

The Wanfu Coal Mine, located in the Juye Coalfield on the Yellow River alluvial plain in Shandong Province (Figure 1), faces unique geological challenges. The mine is overlain by a thick layer of unconsolidated sediments—up to 750 m—composed primarily of clay and sand [14] (Figure 2), underlain by a thin bedrock layer. These conditions. Combined with high water pressure (up to 8.2 MPa) and significant ground stress (exceeding 30 MPa), predispose the mine to WSMF disasters. Furthermore, the region has well-developed fault systems dominated by normal faults, influenced by a complex tectonic stress field [15, 16]. Particularly in the disaster site area, several normal faults are prominent, including F24, F23, FG3, and FD3, all with fault throws exceeding 5 m (Figure 2b).

vol. 31, issue 3 / 2025
pp. 127-135

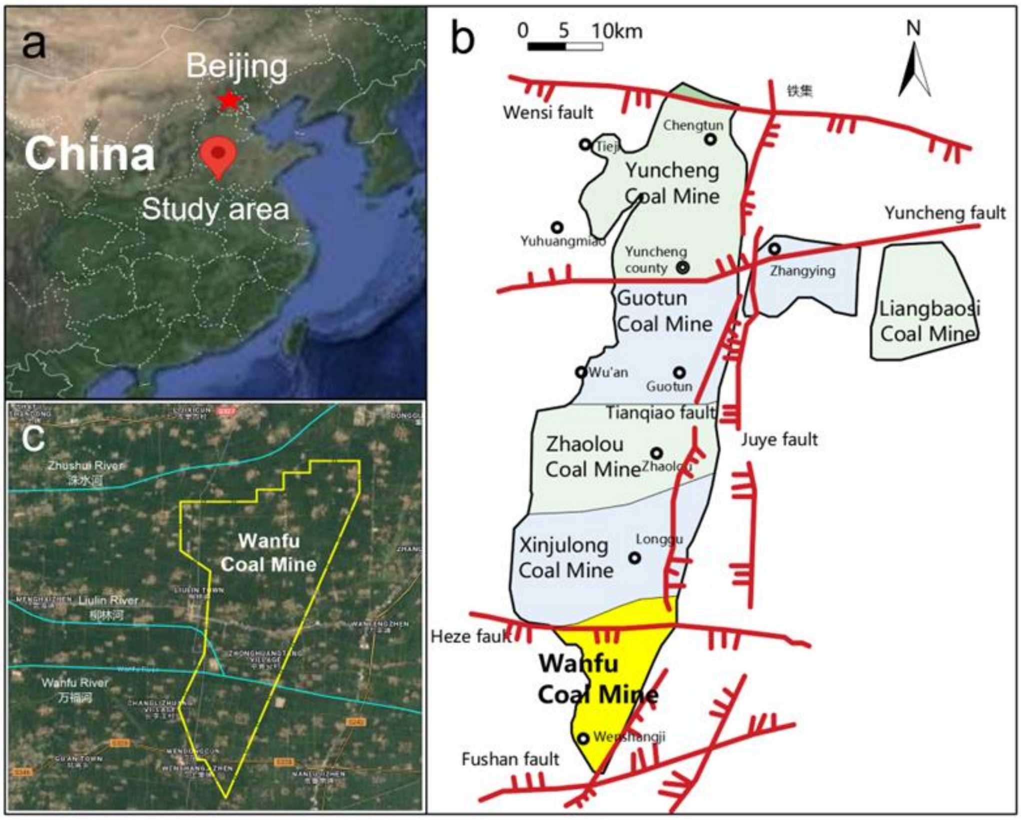

Fig.2. Study area (a) Location of study area (b) Juye Coalfield (c) Wanfu Coal Mine

A notable WSMF disaster occurred on November 2, 2018, in the ventilation inclined shaft of Wanfu Coal Mine. The incident, at a depth of approximately 830 m and with a bedrock thickness of 113.5 m, lead to the loss of one worker and direct economic damages estimated at 7.97 million CNY. During shaft construction, fault zones filled with fractured mudstone were exposed, triggering roof collapse and water inflow. At the time of the disaster, the roof rapidly collapsed within a short period, and the instantaneous rate of water-sand mixture reached 14,580 m³/h. The disaster stabilized after two hours. Post-disaster recovery efforts, completed by December 30, 2018, cleared 2,413 m of tunnels, pumped out 337,000 m³ of water, and removed 22,000 m³ of sand and sediment.

2.2. Construction of 3D model and numerical simulations

The 3D geological model was constructed using Istis.neo (Geovariances Software) based on borehole data. Borehole information, including stratigraphy and lithology, was used to define the spatial distribution of geological features. The geological units parameters including top, bottom and thickness values were used to construct the 3D geological model. Since the deposit is a coal seam and it follows sedimentary horizontal layers, the most appropriate approach was to interpolate each layer by multivariate analysis of top, bottom and thickness of the selected layer:

$$T(x)=Z_2(x)-Z_1 \tag{1}$$

Knowing any two of the three variables Z1(x): top values of the layer, $Z_2(x)$: bottom values of the layer, T(x) can be obtained as the thickness by CoKriging of top and bottom of the layer. In order to use CoKriging, the direct variogram and cross variograms of all variables (Z_1 and Z_2) for all layers are used [17]. The interpolation was conducted using both variables, to estimate the thickness of the layers by weighting top and bottom data points based on their cross spatial correlation. The kriging estimator is expressed as:

$$T^*(x) = \sum_{i=1}^{n} \lambda_{i1} Z_1(x_i) + \sum_{j=1}^{n} \lambda_{j1}\, Z_2(x_j) \tag{2}$$

where $Z^*(x)$ is the thickness estimated value at location x, $Z_1(x_i)$ represents known top values at n nearby locations, $Z_2(x_i)$ represents known bottom values at n nearby locations and $\lambda_{i1},$ are weights determined by solving the kriging system based on the semi variogram models and cross variograms.

The interpolated results were then used to generate a 3D grid representing the subsurface stratigraphy and geological structures, providing a detailed framework for further analysis and simulations.

3. Results

3.1. 3D Model

Using data from 16 boreholes, a three-dimensional model of the study area was constructed. The borehole distribution is shown in Figure 8.

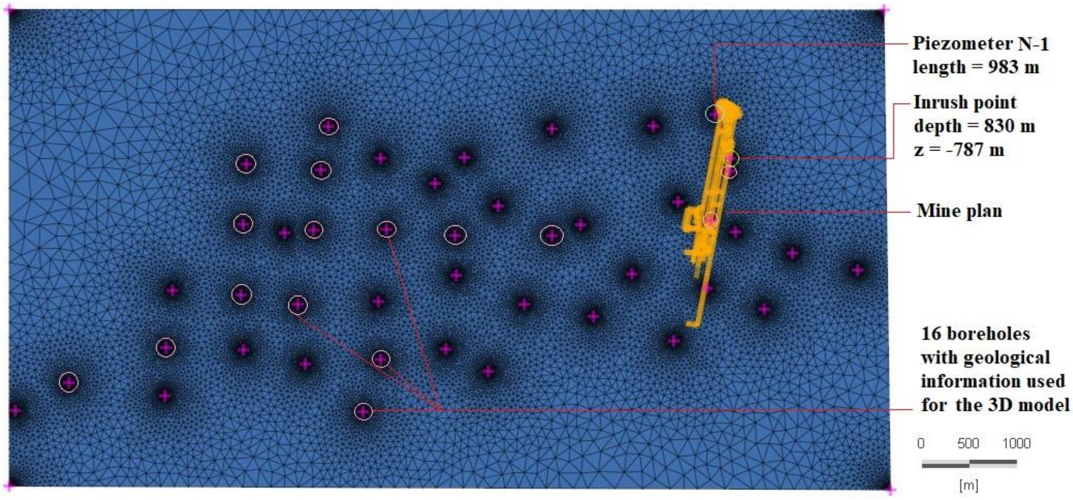

Fig.3. Plan view of boreholes distribution and other information

The result of the geostatistical analysis was the geological model, which means estimation of layer bases and thicknesses for all geological domains. The results are reported below.

Table 1. Geological layers estimated with their boundaries

	Elevation (m)			Thickness (m)		
Layer	**Maximum**	**Minimum**	**Average**	**Maximum**	**Minimum**	**Average**
Surface	43.71	42.73	43.17	786.89	725.66	747.69
Top clay	-682.60	-743.23	-704.52	21.67	1.30	7.02
Top sand (4)	-688.05	-754.68	-711.54	18.90	-9.42	6.41
Top mud (4)	-695.26	-753.33	-717.95	132.17	13.54	64.24
Top sand (3)	-736.64	-845.73	-782.19	135.25	0.00	22.58
Top mud (3)	-740.19	-914.10	-804.77	45.01	3.97	25.16
Top sand (2)	-752.70	-957.89	-829.94	19.95	5.30	10.88
Top mud (2)	-767.04	-965.07	-840.82	70.68	8.22	22.19
Top coal	-780.20	-973.46	-863.01	8.62	5.17	6.53
Top mud (1)	-788.01	-978.91	-869.54	15.78	0.00	3.83
Top sand (1)	-794.56	-980.29	-873.37	36.04	10.47	20.76
Base	-806.00	-1016.33	-894.13	0.00	0.00	0.00

The analysis and visualization focused on key features displayed in the 3D model, such as the geometric morphology and spatial distribution of potential channels (hydraulic conductivity features). The 3D geological model, together with its hydraulic conductivity features, based on geological information was then imported in the software FEFLOW®, which is a finite element simulator of flow dynamics in the subsoil.

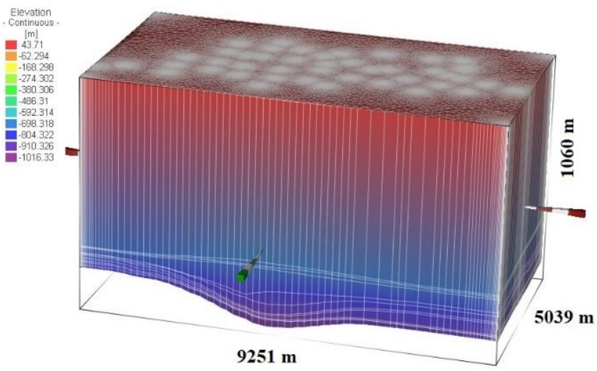

Fig.4 Three-dimensional model of the study area

vol. 31, issue 3 / 2025
pp. 127-135

To each geological layer a characteristic value of hydraulic conductivity was assigned. It is reported in Table 2.

Table 3. Hydraulic conductivities of the different layers

Layer	Hydraulic conductivity (m/d)
Surface	1.05337
Top clay	0.0001
Top sand (4)	0.00494
Top mud (4)	0.02047
Top sand (3)	0.02047
Top mud (3)	0.02047
Top sand (2)	0.02047
Top mud (2)	0.02047
Top coal	0.04363
Top mud (1)	0.00494
Top sand (1)	0.00494
Base	0.00494

By constructing 3D models of geological layers and integrating them with water level data observed during the incident, it is possible to fit and simulate the flow dynamics. This approach provides a means to reverse-engineer and reconstruct the migration pathway, offering crucial insights into the mechanics of water-sand inrush disasters. This modelling process not only enhances our understanding of the specific disaster but also establishes a methodology for analyzing similar events in the future.

In the model, the exact flows measured at the inrush point were inserted as boundary condition, in order to simulate the hydraulic head and pressure drop around the accident point, for different scenarios of channels.

Table 3. Inflow rates inserted as boundary conditions

Step	Time (h)	Inflow rate (m^3/d)
1	0	36
2	10,248.0	36
3	10,248.2	349,920
4	10,261.2	349,920
5	10,261.4	139,200
6	10,263.8	139,200
7	10,264.1	5,712
8	11,835.8	5,712
9	11,836.1	36
10	12,720.0	36

Field estimates indicate that the initial instantaneous maximum water-sand inrush reached approximately 14,580 m^3/h. Two hours after the disaster, the flow rate stabilized. Over the course of two months of emergency response efforts, a total of 21,914 m^3 of sand and slurry was removed, and 337,305 m^3 of water was pumped out. Based on this, the simulated inrush flow rates were set as follows:

a) 14,580 m^3/h (349,920 m^3/d) for 1 hour
b) 5,800 m^3/h (139,200 m^3/d) for 1 hour
c) 238 m^3/h (5,712 m^3/d) for 58 days

The corresponding water-sand flow volumes were calculated as follows: water-sand mixture flow (mainly sand): $14{,}580 + (5{,}800 \times 1.3) = 22{,}120$ m^3 and water (mainly): $238 \times 58 \times 24 = 331{,}296$ m^3. These values closely align with the observed field conditions.

3.2 Numerical simulations

Figure 5 illustrates the monitoring results from various observation wells during the disaster. The data indicate that, following the accident, the water level in Neogene observation well N-1 (located 252° from the disaster site at a distance of 510 m) dropped sharply in a short period, while the water level in Neogene

 vol. 31, issue 3 / 2025
pp. 127-135

observation well N-2 (located 302° from the disaster site at a distance of 1081 m) experienced a slight decrease. In contrast, the water levels in Quaternary and Ordovician observation wells remained largely stable. Specifically, within hours of the accident, the water level in N-1 plummeted from a normal level of -6.24 m to -58.2 m (Figure 7). Additionally, the normal mine water inflow is primarily sourced from the third layer of thin limestone and sandstone aquifers under No. 3 coal seam, with a typical water temperature of approximately 43°C. However, the water temperature during this incident was around 30°C, confirming that the water source originated from the Neogene aquifer. The sand inrush was determined to originate from the Neogene sand layer at a depth of 720–730 m. This layer consists predominantly of fine sand mixed with gravelly coarse sand and yellowish-gray clay.

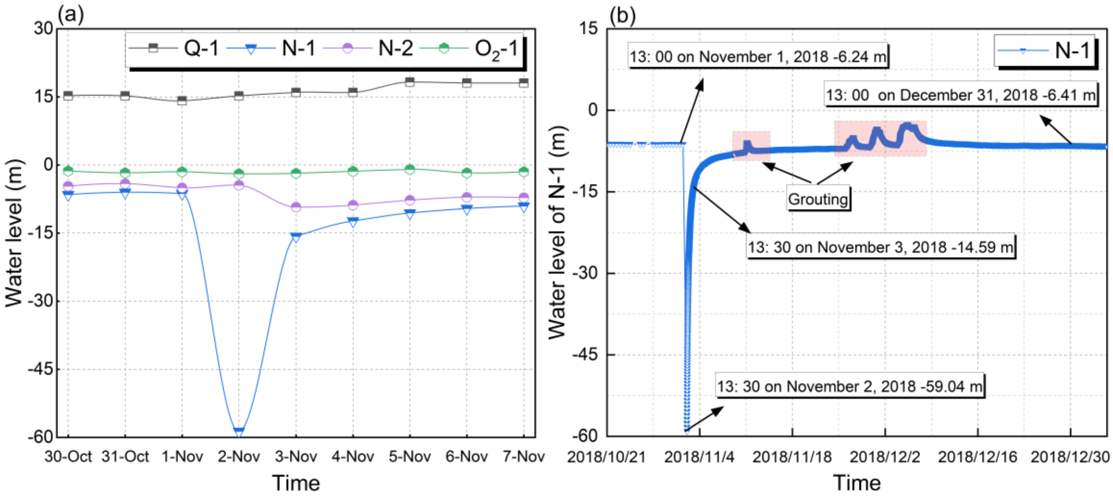

Fig.5. Water levels of each aquifer

According to the 3D modelling of the situation, the presence of these two channel types in the study area is plausible and schematic diagrams of the two types of pathways are presented in Figure 6. The first type of channel may have formed during the mining of the return air incline shaft, where nearly vertical normal faults and caving zones were exposed, directly connecting the water-sand source and triggering the disaster. The second type of channel may be associated with small faults developed on-site. Drilling data indicate the presence of fractured mudstone layers with RQD values of 10%–30%, suggesting that these fractured layers could act as a medium through which multiple vertical pathways connect the water-sand source, leading to the disaster. The plausibility of these two channel types was evaluated through vertical simulation.

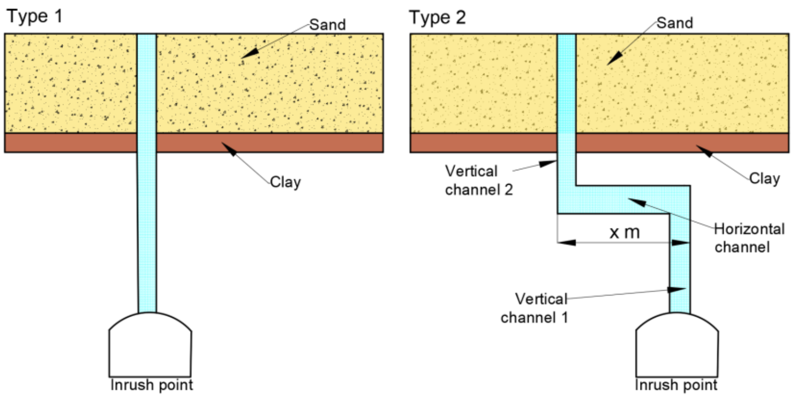

Fig. 6. Schematic diagram of two types of pathways

Starting from the hydrological monitoring borehole N-1, multiple monitoring points were set up at distances of *i m* (*i = 5, 10, 20, 40, 50, 100, 150 m...*). The distance between each monitoring point and the disaster site is *x m* (*x = 510 – i*). The monitoring results are shown in Figure 7. By simulating the water inrush during the disaster, the water level monitoring results of borehole N-1 fell within the range of *i = 100 m* to *150 m*. This indicates that, based on the existing water inrush data and the water level monitoring data of borehole N-1 during the disaster, the actual water-conducting channel on-site is more likely to resemble Type 2. The water level and pressure conditions at the source location under these circumstances are shown in Figure 8.

vol. 31, issue 3 / 2025
pp. 127-135

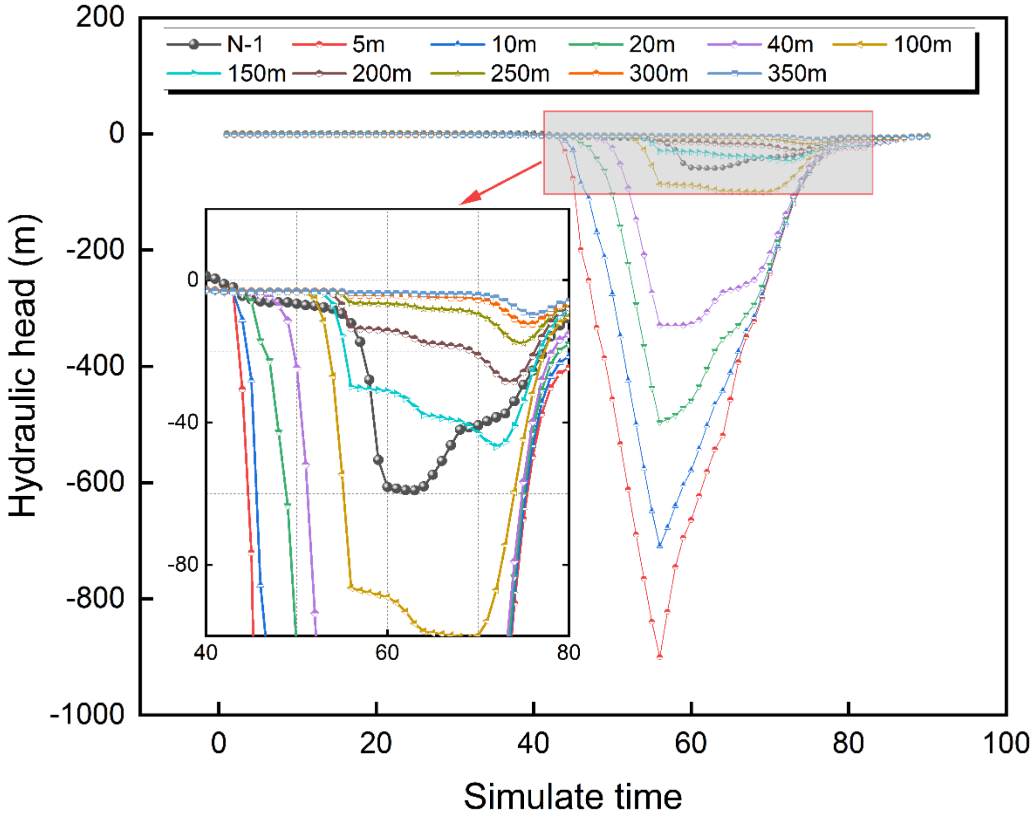

Fig. 7. Distribution of water levels during disasters

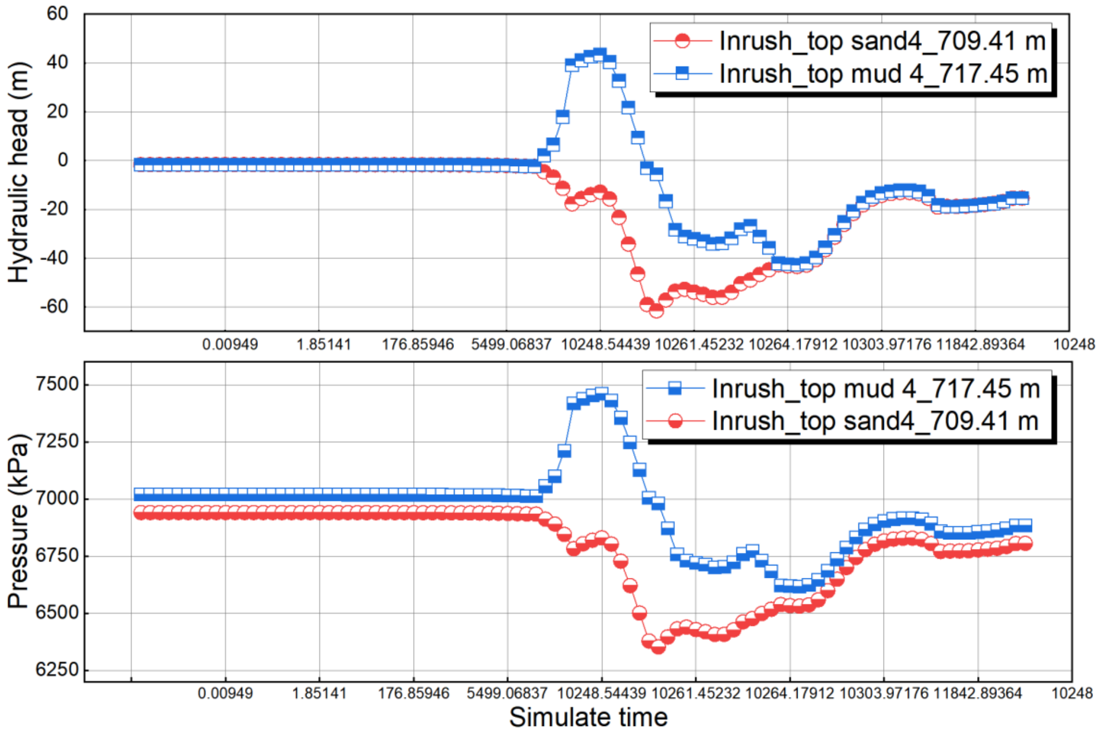

Fig. 8. Hydraulic head and pressure of source layer

4. Conclusions and discussions

A three-dimensional geological model of the study area was constructed through CoKriging method, and simulations were carried out based on the observed water inrush conditions to monitor the spatial distribution of water level changes. The simulations helped to identify the type of water-conducting channel responsible for the disaster. Typically, similar water-sand mixture flow migration disasters can only infer the possible disaster channels based on the disaster site and channels exposed before the disaster occurred.

 vol. 31, issue 3 / 2025
pp. 127-135

Before this particular disaster, a normal fault with a displacement of 0.7 m, a dip angle of 80°, and roof collapse was exposed at the heading of the roadway. Theoretically, the channel should correspond to this fault or the vertically upward-connected collapsed space (Type 1).

However, after the disaster, the water level in a borehole located 510 m from the disaster site showed a significant drop. Based on the drawdown funnel model and assuming a porosity of 0.01 in the overburden layer, achieving such a water level decline would theoretically result in a water inrush volume several times—or even tens of times—the actual volume observed during the disaster.

Vertical simulations were used to verify this hypothesis, and the results suggest that the channel type is more likely Type 2, potentially formed by the combination of multiple channels that contributed to this incident. Given the site conditions, the disaster site itself is located in the pinch-out zone of multiple faults. The overlying strata are fractured, providing water-conducting pathways. Repeated mining in the roadway further caused roof collapse, activating these pathways. Additionally, both faults and collapsed spaces are inclined, meaning that upward-developing water-conducting paths tend to deviate from the vertical direction. Furthermore, the starting point of roadway excavation is close to the hydrological monitoring borehole, suggesting that if a water-conducting pathway existed on-site, its initial activation would likely have begun in this area.

Therefore, based on the numerical simulation results, the water-conducting channel is more inclined toward Type 2, with the main pathway located between the borehole and the disaster site, approximately 350–400 m from the disaster site.

Acknowledgements

The data that support the findings of this study are available from the corresponding author on request.

References

[1] **Sergeant C.J. et al.**, 2022
Risks of mining to salmonid-bearing watersheds, Sci. Adv., vol. 8, no. 26, p. eabn0929, doi: 10.1126/sciadv.abn0929.

[2] **Emberson R., Kirschbaum D., Stanley T.,** 2021
Global connections between El Nino and landslide impacts, Nat Commun, vol. 12, no. 1, p. 2262, doi: 10.1038/s41467-021-22398-4

[3] **Jiang H., Balz T., Li J., Mishra V.,** 2023
Preliminary Investigation of Sudden Ground Subsidence and Building Tilt in Balitai Town, Tianjin City, on 31 May 2023, Remote Sensing, vol. 15, no. 19, p. 4891, doi: 10.3390/rs15194891

[4] **Andreichuk V., Eraso A., Domínguez M.C.,** 2020
A large sinkhole in the Verchnekamsky Potash basin in the Urals, Mine Water and the Environment, vol. 19, no. 1, pp. 2–18, doi: 10.1007/BF02687261

[5] **Brinkmann R., Parise M., Dye D.,** 2008
Sinkhole distribution in a rapidly developing urban environment: Hillsborough County, Tampa Bay area, Florida, Engineering Geology, vol. 99, no. 3, pp. 169–184, doi: 10.1016/j.enggeo.2007.11.020.

[6] **Qian Z., Jiang Z., Guan Y., Yue N.,** 2018
Mechanism and Remediation of Water and Sand Inrush Induced in an Inclined Shaft by Large-Tonnage Vehicles, Mine Water Environ, vol. 37, no. 4, pp. 849–855, doi: 10.1007/s10230-018-0531-3

[7] **Wu X., Yang X., Jing H.,** 2024
Development and experimental validation of analytical models for water and mud inrushes through a filled karst conduit, Sci Rep, vol. 14, no. 1, p. 14969, doi: 10.1038/s41598-024-65930-4

[8] **Liang Y., Sui W., Jiang T., Shen X.,** 2022
Experimental Investigation on the Transport Behavior of a Sand/Mud/Water Mixture Through a Mining-Induced Caving Zone, Mine Water Environ, vol. 41, no. 3, pp. 629–639, doi: 10.1007/s10230-022-00852-z

[9] **Liang Z., Ren T., Ningbo W.,** 2017
Groundwater impact of open cut coal mine and an assessment methodology: A case study in NSW, Int. J. Min. Sci. Technol., vol. 27, no. 5, pp. 861–866, doi: 10.1016/j.ijmst.2017.07.008

vol. 31, issue 3 / 2025
pp. 127-135

[10] **Zhang Q., Jiang Q., Zhang X., Wang D.,** 2019
Model test on development characteristics and displacement variation of water and mud inrush on tunnel in fault fracture zone, Nat Hazards, vol. 99, no. 1, pp. 467–492, doi: 10.1007/s11069-019-03753-7

[11] **Zhang G., Zhang K., Wang L., Wu Y.,** 2015
Mechanism of water inrush and quicksand movement induced by a borehole and measures for prevention and remediation, Bull Eng Geol Environ, vol. 74, no. 4, pp. 1395–1405, doi: 10.1007/s10064-014-0714-5

[12] **Yuan K., Yu B., Zhang M., Yang Y., Yu H.,** 2024
Investigating the dynamics of water-sand mixing inrush in viscous sand layers: insights from laboratory experiments, Nat. Hazards, Jun. 2024, doi: 10.1007/s11069-024-06583-4.

[13] **Xu Y., Luo Y., Li J., Li K., Cao X.,** 2018
Water and Sand Inrush During Mining Under Thick Unconsolidated Layers and Thin Bedrock in the Zhaogu No. 1 Coal Mine, China, Mine Water and the Environment, vol. 37, no. 2, pp. 336–345, doi: 10.1007/s10230-018-0539-8

[14] **Liu H., Li Z., Lv D., Meng Y., Li J., Zhong C.,** 2011
Research the gas geology conditions in Juye coal field, Shandong Province, China, Procedia Engineering, vol. 26, pp. 576–581, doi: 10.1016/j.proeng.2011.11.2208

[15] **Sun X., Qi Z., Zhang Y., Miao C., Zhao C., He M.,** 2023
Failure mechanism and control countermeasures of surrounding rock at deep large section chamber intersection in the Wanfu Coal Mine, J. Mt. Sci., vol. 20, no. 7, pp. 2058–2075, doi: 10.1007/s11629-023-8004-y

[16] **Zhang G. et al.,** 2022
Distribution Law of In Situ Stress and Its Engineering Application in Rock Burst Control in Juye Mining Area, Energies, vol. 15, no. 4, p. 1267, doi: 10.3390/en15041267

[17] **Rivoirard J.,** 1990
A review of lognormal estimators for in situ reserves, Math Geol, vol. 22, no. 2, pp. 213–221, Feb. 1990, doi: 10.1007/BF00891825